Correlated cryogenic photoactivated localization microscopy and electron cryotomography

Yi-Wei Chang[1,2], **Songye Chen**[1,2], **Elitza I. Tocheva**[1], **Anke Treuner-Lange**[3], **Stephanie Löbach**[3], **Lotte Søgaard-Andersen**[3], and **Grant J. Jensen**[1,2,4]

[1]Division of Biology and Biological Engineering, California Institute of Technology, Pasadena, USA.

[2]Howard Hughes Medical Institute, Pasadena, USA.

[3]Max Planck Institute for Terrestrial Microbiology, Marburg, Germany.

Abstract

Electron cryotomography (ECT) produces three-dimensional images of cells in a near-native state at macromolecular resolution, but identifying structures of interest can be challenging. Here we describe a correlated "cryo-PALM"-ECT method for localizing objects within cryotomograms to beyond the diffraction limit of the light microscope, and use it to identify multiple and new conformations of the dynamic type VI secretion system in the crowded interior of *Myxococcus xanthus*.

Electron cryotomography (ECT) allows large macromolecular complexes to be visualized directly within intact cells[1]. Because cells are preserved in a near-native state, and reconstructions exhibit "macromolecular" resolution (~4 nm), some complexes can be identified simply by their known shapes[2]. Unfortunately this requires prior knowledge of a macromolecule's morphology, association with other macromolecules, and/or subcellular location. It is therefore of great interest to expand this technique to characterize structures that are smaller, dynamic, or less-well characterized.

One way to identify objects of interest in cryotomograms is through correlated fluorescence light (FLM) and electron microscopy (EM)[3,4]. In this approach, proteins of interest are fused to fluorophores and coarsely localized by FLM. The same samples are then imaged by ECT and the two images superposed. While powerful, correlated FLM-ECT approaches have

limitations. FLM is best carried out at room temperature to allow use of oil immersion lenses with high numerical aperture (NA~1.4), but movement can prevent correlation of subcellular structures. As a result, only relatively static structures like bacterial stalk cross-bands[5] or eukaryotic focal adhesions[6] can be studied this way. Alternatively, cells can be chemically fixed before imaging, but this can introduce artifacts[7,8]. Cells can also be plunge-frozen prior to FLM and imaged cold (~80 K), but this severely limits fluorescence resolution since long-working-distance air objectives (NA~0.7) are then required. Intriguingly, several super-resolution microscopy techniques have been described recently, including STORM[9], PALM[10], and FPALM[11]. These techniques have dramatically improved fluorescence resolution, allowing single-molecule localization, but none has been performed under cryogenic conditions. Here we report the development of a super-resolution method that can be applied to frozen samples ("cryo-PALM"), allowing dynamic cellular objects to be localized within cryotomograms.

PALM relies on sequential laser-induced activation and inactivation of photoactivatable fluorophores[10]. To perform PALM on frozen EM grids, we added a multi-color laser to our correlative cryo-FLM-ECT system[3]. Normally, methods such as PALM rely on total internal reflection (TIRF) illumination to reduce background, but since imaging frozen EM grids requires an air objective lens, we used epi-illumination. Fortunately, because ECT samples are thin (< 500 nm) there was little background fluorescence and the signal-to-noise ratio was sufficient for single-molecule localization after sample vibration and drift were minimized (Online Methods).

In ECT living cells are preserved by vitrification without chemical fixation or permeabilization. This limits possible cryo-PALM probes to those that can be incorporated into living cells, such as genetically-encoded photoactivatable fluorescent proteins (PA-FPs). Since low temperature drastically reduces the photobleaching rate of fluorescent proteins[12], and might also alter their photoconversion behaviors, we screened PA-FPs for activation and inactivation at 80 K. We chose only monomeric candidates in order to avoid PA-FP polymerization[13]. Surprisingly, most PA-FPs tested did not respond, or responded very weakly, to illumination by the activation/conversion laser (Supplementary Fig. 1). Only PA-GFP maintained its photoactivatable behavior at 80 K. As at room temperature, photoconversion was reliably triggered by a 488-nm laser, and photoactivation could be accelerated by adding a 405-nm laser. With the long-working-distance air objective (NA 0.7) and the presumably slower photobleaching rate at 80 K[12], the average number of photons collected per PA-GFP molecule was 206 (Supplementary Fig. 2).

One concern with cryo-PALM is that exposure to the intense laser might warm the sample above 135 K, causing vitreous ice to crystallize and denature the sample[14]. To examine this, we exposed vitrified samples on EM grids to a laser with sufficient energy for PA-GFP photoconversion (300 W/cm^2) and then imaged the grids by ECT. The laser exposure caused small crystals to form within the amorphous ice surrounding cells (Supplementary Fig. 3a), but cytoplasmic structures were not affected perceptibly, likely because the crowded cellular interior served as a natural cryo-protectant. Adding 5% Ficoll PM 70 as a cryo-protectant and reducing the total laser exposure time to less than 300 seconds per target reduced ice crystallization considerably (Supplementary Fig. 3b). Residual ice crystallization and

devitrification were fully overcome by adding 10% Ficoll PM 70 and 10% ethylene glycol and pulsing the exposure, allowing 60 seconds of heat dissipation between each 60-second period of laser illumination (Supplementary Fig. 3c).

Widespread in Gram-negative bacteria, the type VI secretion system (T6SS) is a virulence-associated nanomachine that translocates inhibitors into prey cells[15,16]. In *Vibrio cholerae* the T6SS forms highly dynamic intracellular tubes[17]. Through cycles of sheath extension, contraction and disassembly, these tubes deliver protein effectors into adjacent target cells. Time-lapse FLM has revealed that the T6SS assembles within tens of seconds in a wide range of subcellular locations, and then contracts and disassembles in a similar time frame. Identification of T6SS structures in cryotomograms is therefore complicated by their highly dynamic nature and random localization within the cell. In our previous study characterizing the T6SS in *Vibrio cholerae* by ECT, mutant strains and purified sheaths needed to be imaged in order to identify which ultrastructure was the T6SS[17].

To characterize the T6SS in a second species, we chose *Myxococcus xanthus*, a model bacterial predator whose genome has been reported to encode all 13 core proteins of the T6SS[18]. We first tried to identify the T6SS in *M. xanthus* through a conventional correlated cryo-FLM-ECT approach using a mutant strain containing a deletion of the gene encoding the sheath protein VipA (also known as TssB) (Δ*vipA*) and expressing a functional VipA-GFP fusion protein (Supplementary Figs. 4 and 5a). Unfortunately, the limited resolution of cryo-FLM gave a broad fluorescence signal that, in the crowded interior of the bacterial cell, often ambiguously spanned a variety of candidate structures in cryotomograms (Supplementary Fig. 5b). To overcome this problem, we performed correlated cryo-PALM-ECT using the mutant expressing VipA-PA-GFP. We localized VipA-PA-GFP molecules in frozen-hydrated cells on EM grids by cryo-PALM (Supplementary Fig. 5c). We then imaged locations with high cryo-PALM signal density at high resolution by ECT. The overall imaging process is demonstrated in Supplementary Movie 1 (with 5% Ficoll PM 70) and Supplementary Movie 2 (with 10% Ficoll PM 70 and 10% ethylene glycol and pulsed laser exposure). In nearly every case (17/20), we observed a tubular structure in the location of VipA-PA-GFP signals. The three signals that did not correlate with a tubular structure likely corresponded to just-disassembled T6SSs whose fluorescent tags were still co-localized. We found that the structure of the T6SS sheath in *M. xanthus* is similar to that reported for *V. cholerae*, and we observed both extended ("loaded") and contracted ("fired") conformations (Fig. 1). Extended tubes exhibited filled lumens (Fig. 1c) and had an average length of 608 ± 75 nm and diameter of 12.6 ± 0.6 nm (n=12). Contracted tubes had clear lumens (Fig. 1f) and an average length of 287 ± 62 nm and diameter of 14.7 ± 0.7 nm (n=9).

One cryo-PALM focus identified a very short (60 nm) filled tube, which was likely a T6SS in an early stage of assembly (Fig. 2a–d, Supplementary Movie 2). The width of this tube matched that of the other extended tubes, suggesting that the inner rod and outer sheath of the T6SS form concomitantly rather than sequentially. Another cryo-PALM focus superposed on a contracted tube bent approximately one-quarter length from its membrane-proximal end (Fig. 2e). Interestingly, we observed an additional layer associated with the tube on one side of the bend (Fig. 2f–i). The tube diameter was identical to that of contracted T6SS sheaths. It therefore likely represents an intermediate in the disassembly process of the

sheath after contraction, raising the question of whether the additional layer is ClpV, the AAA-ATPase known to disassemble T6SS sheaths[19,20]. Demonstrating the utility of correlated cryo-PALM-ECT, this bent sheath was identifiable as a T6SS despite being surrounded by a variety of other tubular structures (Fig. 2j–o).

Correlated cryo-PALM-ECT brings together two of the most powerful light and electron microscopy techniques. By precisely localizing the fluorescent tag on a cellular object by cryo-PALM and then resolving the higher-resolution molecular structure of the object itself by ECT, correlated cryo-PALM-ECT should allow numerous dynamic molecular machines to be structurally characterized *in vivo*, and, importantly, without fixation artifacts. Once the typical structures of an object are known, many will then be recognizable by their morphologies alone in cryotomograms of fully wildtype cells (without any tags at all). The cryoprotectant properties of different cytoplasms will likely vary, however, so the laser pulsing may need to be optimized for each species. The cryo-PALM setup described here had a maximum lateral position error of ~160 nm (Supplementary Table 1), easily allowing us to identify T6SS structures (11–15 nm wide and 200–500 nm long in 2-dimensional projections). Our identification of an unusually short T6SS sheath just 12 nm wide and 60 nm long demonstrates the power of this method to identify smaller structures as well. Future development of brighter and longer-lasting cryo-photoactivatable fluorophores, higher-NA cryo-FLM objectives, more stable cryo-stages, and better tools for transfer of samples and correlation of images could further increase the power of this approach. The use of a cryo-fluorophore ten times brighter and lasting ten times longer before bleaching at 80 K than PA-GFP, imaged with a 100× long-working-distance air objective with NA~0.8, would increase the precision to better than 2 nm, sufficient to pinpoint the location of almost any macromolecule within the cell.

ONLINE METHODS

Cell growth

M. xanthus strains used in this study are listed in Supplementary Table 2. The strains were grown at 32 °C in CTT medium or on CTT agar plates supplemented with kanamycin (40 μg/ml)[21]. *E. coli* strains were grown in LB broth at 37 °C. Plasmids were propagated in *E. coli* TOP10 *(F-, mcrA, Δ(mrr-hsdRMS-mcrBC), φ80lacZΔM15, ΔlacX74, recA1, araD139, Δ(ara, leu) 7679, galU, galK, rpsL, endA1, nupG).*

M. xanthus strain construction

The in-frame deletion mutations were generated in the WT strain DK1622[22] using standard methods[23] and plasmids pSlo4 (to generate strain SA5716 (Δ*vipA*=Δ*MXAN4807*)) and pAK88 (to generate SA5707 (ΔT6SS=Δ*MXAN4800−4813*)). Strains SA4137 (Δ*vipA*/P$_{pilA}$−*vipA*-GFP) and SA5718 (Δ*vipA*/P$_{pilA}$−*vipA*-PA-GFP) were generated by electroporation of plasmids pMAT36 and pSlo5, which encode VipA-GFP and VipA-PA-GFP, respectively, and integrate into the Mx8 *attB* site, into SA5716. Assays for motility[24] and development[21] were carried out as described.

Plasmid construction

Plasmid pSlo2 was generated by amplification of the *vipA* gene without its stop codon using primers oVipA1 and oVipA3 (see Supplementary Table 3 for primer sequences) and *M. xanthus* chromosomal DNA as template. The product was ligated into pTP100 by *Xba*I-*Bam*HI digestion. GFP was amplified from pFCrGFP (BioCat) using primers oGFP1 and oGFP2. PA-GFP was amplified from pRSETA-PA-GFP (Addgene 11911) using primers oPAGFP1 and oPAGFP2. The GFP and PA-GFP fragments were cloned into pSlo2 by *Bam*HI- *Kpn*I digestion to generate pMAT36 and pSlo5, which integrate into the Mx8 phage *attB* site and express VipA-GFP and VipA-PA-GFP, respectively, from the *pilA*-promoter. In the two fusion proteins GFP and PA-GFP are separated from VipA by an Ala-Ala-Ala-Gly-Gly-Gly linker.

To generate the in-frame deletion of *vipA,* pSlo4 was constructed by cloning the upstream (primer pair mxan4807AB) and downstream (primer pair mxan4807CD) regions of *vipA* into vector pBJ114[25]. This deletion extends from nucleotide 31 to 465 of *vipA* (*vipA* has a total length of 495 bp). To generate the in-frame deletion of all T6SS-encoding genes *MXAN4800–4813*[18], plasmid pAK88 was generated by cloning the upstream (primer pair mxan4800AB) and downstream (primer pair mxan4813CD) regions of the T6SS gene cluster into vector pBJ114[25]. The resulting deletion extends from codon 26 of *MXAN4800* to codon 867 of *MXAN4813*.

Immunoblot analysis for M. xanthus T6SS activity

To determine whether the *M. xanthus* T6SS is active, the accumulation of hemolysin-coregulated protein (Hcp) in the culture supernatant[26] of an exponentially growing WT strain, a mutant containing a deletion of the entire T6SS gene cluster including the gene encoding Hcp (ΔT6SS), and a mutant containing a deletion of the gene encoding the core protein VipA (Δ*vipA*) was monitored by immunoblot analysis. The SDS-PAGE gel for the α-Hcp immunoblot was loaded with total cell extracts from 2.5×10^7 cells and concentrated cell-free supernatants from 1.5×10^{10} cells. To prepare cell-free supernatants, cultures of exponentially growing *M. xanthus* cells at OD_{550nm} 0.9–1.1 were used. Cells were harvested by centrifugation and the supernatant filtered through a 0.22 μm sterile filter. Precipitation of the proteins in the filtered supernatant was performed using TCA-DOC precipitation. Briefly, 1/100 volume of 2% sodium deoxycholate (DOC) was added and the solution incubated at 4 °C for 30 min. Afterward TCA was added to a final concentration of 10% and the solution was incubated at 4 °C for another 16 hr. Protein precipitate was sedimented by centrifugation (15 min, 10,000 g). The collected pellet was washed twice with acetone and then resuspended in SDS-PAGE loading buffer. Immunoblotting was performed using standard procedures with rabbit α-Hcp (Eurogentec, SY2563, 1:500) and peroxidase-conjugated goat α-rabbit IgG secondary antibodies (Sigma-Aldrich, A8275, 1:10,000) following the recommendations of the manufacturer. Rabbit antiserum against Hcp was generated by Eurogentec, using a mixture of the peptides REAGSGLATGRRQYEG and ITQGGVTHEDTWDTQR, corresponding to residues 44–59 and 148–163 of the Hcp protein, respectively. The blot was developed using Luminata Western HRP substrate (Millipore, WBLUF0100). Hcp was detected in total cell extract as well as in the cell-free supernatant of WT cells, only in the total cell extract of the Δ*vipA* mutant, and in neither

fraction in the ΔT6SS mutant (Supplementary Fig. 4), indicating that the *M. xanthus* T6SS is active. The ΔT6SS and Δ*vipA* mutants were indistinguishable from WT with respect to growth, motility, fruiting body formation and sporulation. To detect VipA-PA-GFP and VipA-GFP, the α-Hcp blot was stripped (Restore PLUS Western blot stripping buffer; Thermo Scientific, 46430), and the blot probed with mouse α-GFP primary (Roche, 11814460001, 1:2000) and α-mouse IgG secondary antibodies (DakoCytomation, P0260, 1:2000) and developed as described.

Enhancing cryo-FLM stage stability

In the cryo-FLM setup, liquid nitrogen (LN) is continuously pumped into the stage in order to maintain the sample at 80 K. The flow and boiling of LN cause vibrations in the stage. To control this problem, the insulation of the cryo-FLM stage was improved by introducing a 1-cm-thick poly(methyl methacrylate) plate as a lid to reduce heat loss through the condenser hole while preserving transparency for light traveling through the condenser aperture into the cryo-stage (Supplementary Fig. 6). The resulting slower heat exchange suppressed LN boiling and reduced its flow. The slight residual stage drift during data recording could be corrected by registering fluorescent fiducial beads, as in the room temperature PALM method[10].

Photoactivation/photoconversion test of PA-FPs in cells at 80 K

E. coli BL21(DE3) cells harboring plasmid pRSETA-PA-GFP, pRSETA-Dendra2, pRSETA-Dronpa, pRSETA-mEosFP2, pRSETB-PA-mRFP1, pET28a-PS-CFP2, or pBAD/HisB-PA-mCherry1 were first grown to an OD_{600} of 0.6 and expression of PA-FPs was then induced with 1 mM isopropyl β-D-1-thiogalactopyranoside or 0.2% (w/v) L-arabinose for 2 hours. The cells were applied to coverslips and photoactivation/photoconversion of the PA-FPs was confirmed with room temperature FLM using a 100× oil immersion objective lens. Exposures of 1–3 seconds using a mercury lamp with a DAPI filter set (Semrock DAPI-1160A-NTE) were used to trigger the photoactivation/photoconversion. Exposures of 1–3 seconds through a FITC (Semrock FITC-3540B-NTE) or a TxRed (Semrock TxRed-4040B-NTE) filter set were used to record green or red fluorescent signals, respectively. Aliquots from the same batches of cells were then plunge-frozen on EM grids and loaded into the cryo-FLM setup (detailed procedure is described in the next section) for imaging at 80 K. Exposures of 0.1–10 seconds using a 405-nm laser with 100–1000 W/cm^2 of power at the sample plane were used in an attempt to trigger photoactivation/photoconversion. Exposures of 0.1–1 seconds using a 488-nm or 561-nm laser with 100–1000 W/cm^2 of power at the sample plane were used to record green or red fluorescent signals.

Correlated cryo-PALM-ECT

M. xanthus SA5718 cells were grown to an OD_{550nm} of 0.4. 10-nm colloidal gold (Sigma-Aldrich) pretreated with bovine serum albumin was added to the cells for fiducial markers during tomogram reconstruction. 200-nm orange fluorescent FluoSpheres (Life Technologies) were added to the cells for stage drift correction in cryo-PALM and also for use as landmarks for correlating FLM and EM images. 5% Ficoll PM 70 (Sigma-Aldrich) or

10% Ficoll PM 70 with 10% ethylene glycol (Sigma-Aldrich) were added as cryo-protectants for laser exposure. 3 μl of the resulting sample was pipetted onto a freshly glow-discharged Quantifoil gold London-finder EM grid (Quantifoil Micro Tools GmbH) and plunge-frozen in a liquid ethane propane mixture using an FEI Vitrobot (FEI Company). Frozen grids were then loaded into Polara EM cartridges, transferred into a cryo-FLM stage (FEI Cryostage[2], modified to hold Polara EM cartridges)[3] mounted on a Nikon Ti inverted microscope, and imaged using a 60× extra-long working distance air objective (Nikon CFI S Plan Fluor ELWD 60× NA 0.7 WD 2.62-1.8 mm). Photoactivation and photobleaching of VipA-PA-GFP were first triggered solely by a 488-nm laser to produce blinking signals. An additional 405-nm laser was subsequently added when needed to increase the density of blinking signal. The laser illumination system (Prairie Technologies) was configured to provide 405nm, 488nm and 561nm at 100mW. The 488-nm laser was adjusted to 0.2–0.4 mW of power at the sample plane, spread over an area of ~100 μm^2 to yield 200–400 W/cm^2. The 405-nm laser was adjusted to 10–20 μW of power at the sample plane, spread over an area of ~100 μm^2 to yield 10–20 W/cm^2. These ranges of laser intensities were chosen to avoid ice crystallization on the frozen sample but still be strong enough to excite bright signals and bleach before the stage drifted notably. The images were taken by a QuantEM 512SC electron multiplying CCD camera (Photometrics) using Nikon NIS-Elements Ar software (Nikon). The data recording frame rate was 100 – 300 ms/frame. The laser exposure on each target was limited to total 300 seconds and fragmented into 60-second segments flanked by 60-second rests. Approximately 500 – 1,000 frames were typically recorded to generate the super-resolution images for VipA-PA-GFP. The "descriptor-based registration" plugin[27] of ImageJ software (National Institutes of Health) was used to correct sample drift in cryo-PALM movies. The RapidSTORM software package[28] was used to analyze cryo-PALM image stacks and generate super-resolution reconstruction images. The total number of photons detected per activated single PA-GFP molecule for Figures 1 and 2 in main text and Supplementary Movie 1 and 2 are plotted in Supplementary Figure 2. The acquisition time for each frame of the image stack (τ_{frame}), total number of acquired frames in the image stack (F_{total}), total number of molecules localized in the image stack (M_{total}), maximum acceptable position error for inclusion in the final image (($\sigma_{x,y})_{max}$), and number of localized molecules composing the final image (M_{image}) for Figures 1 and 2 in the main text and Supplementary Movie 1 and 2 are summarized in Supplementary Table 1. The position error $\sigma_{x,y}$ for each single molecule was estimated as previously reported[29], with:

$$(\sigma_{x,y})^2 = \frac{s^2 + a^2/12}{N} + \frac{8\pi s^4 b^2}{a^2 N^2}$$

where N is the number of photons recorded in the fitted point spread function (PSF), a is the pixel size, b is the background noise and s is the standard deviation of the PSF.

After cryo-PALM imaging, EM cartridges containing frozen grids were stored in liquid nitrogen and maintained at 123 K or less throughout transfer into and imaging in an FEI Tecnai G2 Polara 300 keV FEG transmission electron microscope (FEI Company) equipped with a Gatan energy filter (Gatan) and a Gatan K2 Summit direct detector (Gatan). Tabs on

the finder-grid were used to locate the cells imaged by cryo-PALM. Energy-filtered tilt-series of images on individual cells were collected automatically from −60° to +60° at 1° intervals using the UCSF Tomography data collection software[30] with total dosage of 180 $e^-/Å^2$ and a defocus of −10 μm. Three-dimensional reconstructions and segmentations were produced with IMOD[31].

To overlay the cryo-PALM signals onto cryotomograms, low magnification EM images of the target cells were acquired to locate surrounding fluorescent polystyrene beads. Cryo-PALM images were then rescaled to match the EM images based on the locations of the beads by using the GNU image manipulation program (GIMP) (http://www.gimp.org). The precision of superimposition of the beads between FLM/EM in Supplementary Movie 1 is shown in Supplementary Figure 7. Central slices of cryotomograms were superposed onto low-resolution EM images by aligning the edges of cells and the holes of the EM grid by using GIMP.

Supplementary Material

Refer to Web version on PubMed Central for supplementary material.

ACKNOWLEDGEMENTS

REFERENCES

1. Gan L, Jensen GJ. Q. Rev. Biophys. 2012; 45:27–56. [PubMed: 22082691]

2. Nickell S, Kofler C, Leis AP, Baumeister W. Nat. Rev. Mol. Cell Biol. 2006; 7:225–230. [PubMed: 16482091]

3. Briegel, A., et al. Methods in Enzymology. Jensen, GJ., editor. Vol. Vol. 481. Academic Press: 2010. p. 317-341.

4. Plitzko JM, Rigort A, Leis A. Curr. Opin. Biotechnol. 2009; 20:83–89. [PubMed: 19345086]

5. Schlimpert S, et al. Cell. 2012; 151:1270–1282. [PubMed: 23201141]

6. Patla I, et al. Nat. Cell Biol. 2010; 12:909–915. [PubMed: 20694000]

7. Pilhofer, M.; Ladinsky, MS.; McDowall, AW.; Jensen, GJ. Methods Cell Biol. Müller-Reichert, T., editor. Vol. Vol. 96. Academic Press; 2010. p. 21-45.

8. Pilhofer M, et al. Environ. Microbiol. 2014; 16:417–429. [PubMed: 24118768]

9. Rust MJ, Bates M, Zhuang X. Nat. Methods. 2006; 3:793–796. [PubMed: 16896339]

10. Betzig E, et al. Science. 2006; 313:1642–1645. [PubMed: 16902090]

11. Hess ST, Girirajan TPK, Mason MD. Biophys. J. 2006; 91:4258–4272. [PubMed: 16980368]

12. Schwartz CL, Sarbash VI, Ataullakhanov FI, Mcintosh JR, Nicastro D. J. Microsc. 2007; 227:98–109. [PubMed: 17845705]

13. Landgraf D, Okumus B, Chien P, Baker TA, Paulsson J. Nat. Methods. 2012; 9:480–482. [PubMed: 22484850]

14. Dubochet J, McDowall AW. J. Microsc. 1981; 124:3–4.

15. Russell AB, et al. Nature. 2011; 475:343–347. [PubMed: 21776080]

16. Pukatzki S, et al. Proc. Natl. Acad. Sci. USA. 2006; 103:1528–1533. [PubMed: 16432199]

17. Basler M, Pilhofer M, Henderson GP, Jensen GJ, Mekalanos JJ. Nature. 2012; 483:182–186. [PubMed: 22367545]

18. Konovalova A, Petters T, Søgaard-Andersen L. FEMS Microbiol. Rev. 2010; 34:89–106. [PubMed: 19895646]

19. Bonemann G, Pietrosiuk A, Diemand A, Zentgraf H, Mogk A. EMBO J. 2009; 28:315–325. [PubMed: 19131969]

20. Basler M, Mekalanos JJ. Science. 2012; 337:815–815. [PubMed: 22767897]

21. Søgaard-Andersen L, Slack FJ, Kimsey H, Kaiser D. Genes Dev. 1996; 10:740–754. [PubMed: 8598300]

22. Kaiser D. Proc. Natl. Acad. Sci. USA. 1979; 76:5952–5956. [PubMed: 42906]

23. Shi X, et al. J. Bacteriol. 2008; 190:613–624. [PubMed: 17993514]

24. Shi W, Zusman DR. Proc. Natl. Acad. Sci. USA. 1993; 90:3378–3382. [PubMed: 8475084]

25. Julien B, Kaiser AD, Garza A. Proc. Natl. Acad. Sci. USA. 2000; 97:9098–9103. [PubMed: 10922065]

26. Silverman JM, Brunet YR, Cascales E, Mougous JD. Annu. Rev. Microbiol. 2012; 66:453–472. [PubMed: 22746332]

27. Preibisch S, Saalfeld S, Schindelin J, Tomancak P. Nat. Methods. 2010; 7:418–419. [PubMed: 20508634]

28. Wolter S, et al. Nat. Methods. 2012; 9:1040–1041. [PubMed: 23132113]

29. Thompson RE, Larson DR, Webb WW. Biophys. J. 2002; 82:2775–2783. [PubMed: 11964263]

30. Zheng SQ, et al. J. Struct. Biol. 2007; 157:138–147. [PubMed: 16904341]

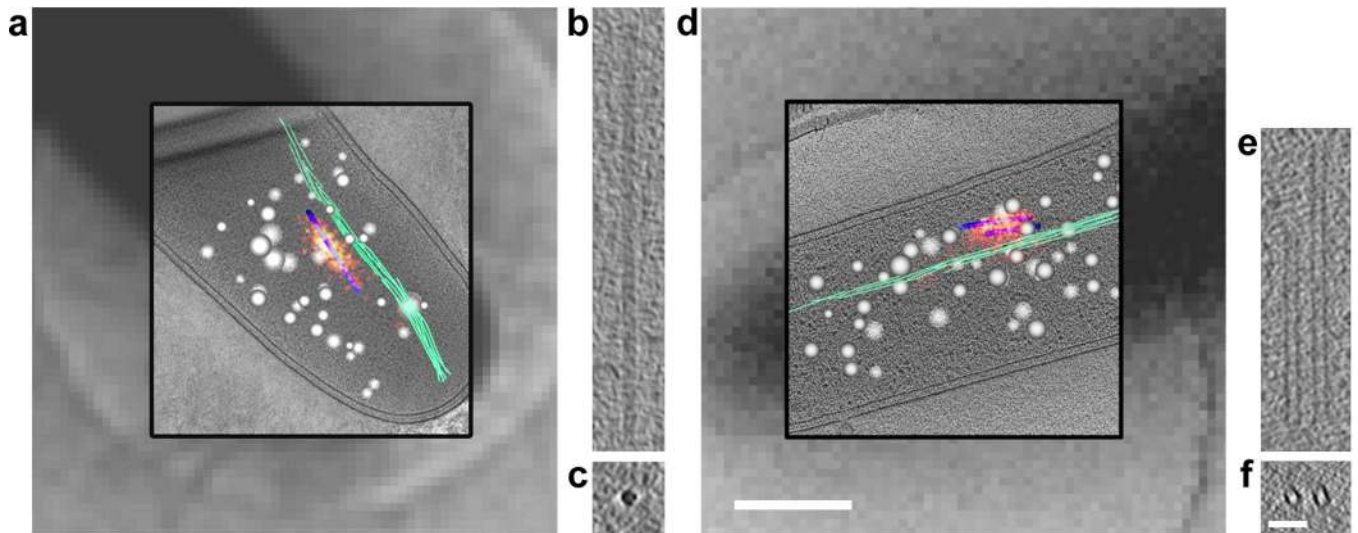31. Kremer JR, Mastronarde DN, McIntosh JR. J. Struct. Biol. 1996; 116:71–76. [PubMed: 8742726]

Figure 1.
Extended and contracted conformations of the T6SS sheath in *M. xanthus* visualized by correlated cryo-PALM-ECT. (**a**, **d**) Low-resolution EM images (grayscale background), cryo-PALM images (red and yellow foreground), slices from high-resolution 3-D cryotomograms (grayscale foreground), and segmentations of cellular structures (blue - tubular structures, green - filament bundles, white - spherical granules) superposed. The cryo-PALM images reveal VipA-PA-GFP localization (red: low; yellow: high precision), identifying the tubular structures as T6SSs. Scale bar in **d** 400 nm. (**b**, **e**) Tomographic slices through the tubular structures (blue) in **a**, **d** showing extended and contracted T6SS sheaths, respectively. (**c**, **f**) Cross-sectional views of **b** and **e**, respectively. Scale bar in **f** 50 nm (applies to **b**, **c**, **e**, **f**).
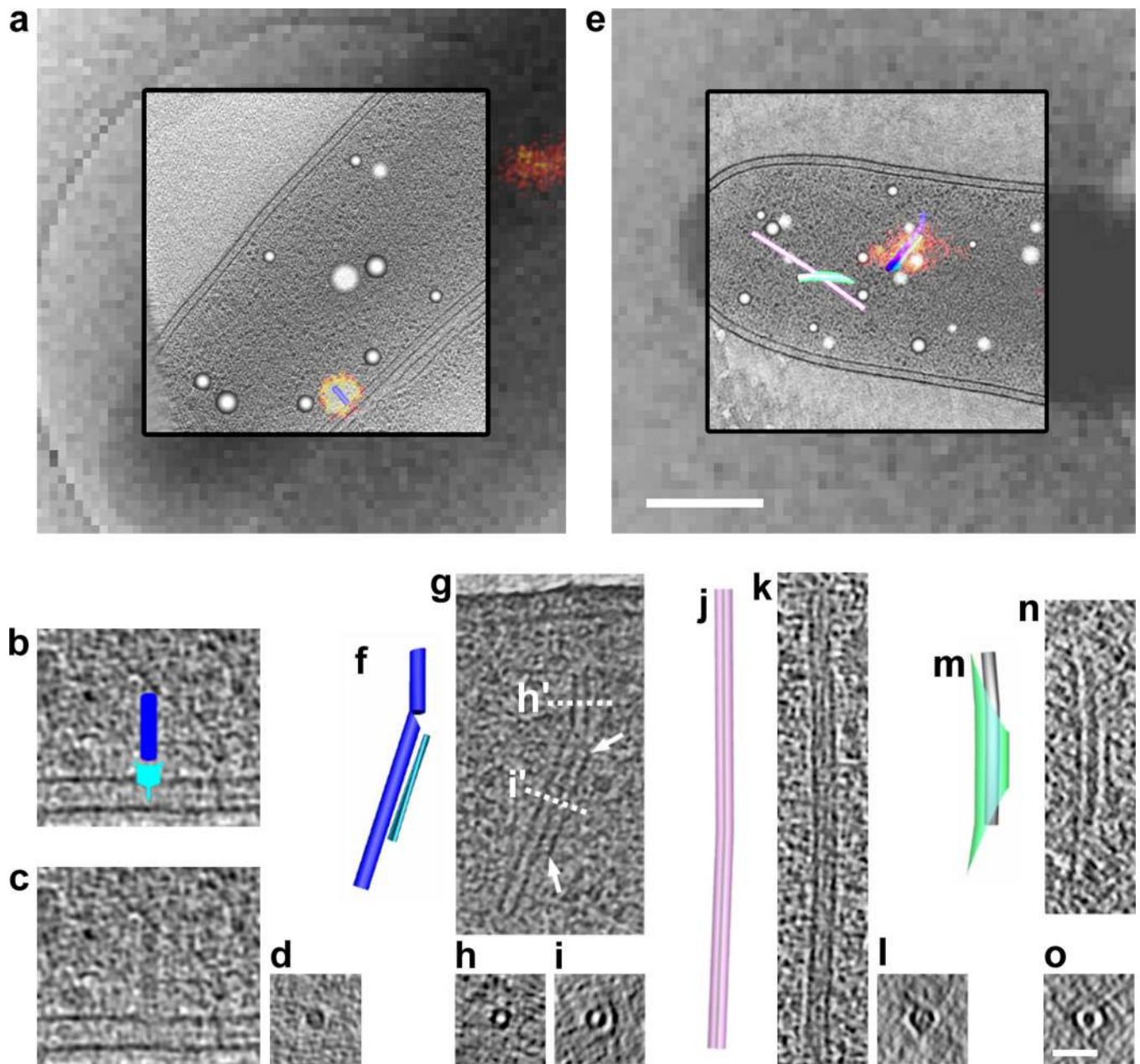
Figure 2.
New T6SS structures identified by correlated cryo-PALM-ECT. (**a**) A very short loaded
T6SS structure with baseplate attached to membrane. Superposed low-resolution EM image,
cryo-PALM signal, high-resolution cryotomographic slice, and object segmentations as in
Figure 1. (**b**) Tomographic slice through the tubular structure corresponding to the
segmentation model shown in **a**. Features of the T6SS highlighted in blue (sheath) and cyan
(baseplate). (**c**) Tomographic slice in **b** without highlights. (**d**) Cross-section view of the
T6SS sheath in **c**. (**e**) A bent T6SS structure with additional sheet, distinguished from other
tubular structures in the vicinity. Segmentation of the cryotomogram shows different tubular
structures (individually colored blue, pink, and green) and spherical granules (white). Scale

bar in **e** 400 nm (applies to **a**, **e**). (**f**, **j**, **m**) Segmented models of tubular structures shown in **e**. (**g**, **k**, **n**) Tomographic slices through the tubular structures corresponding to the segmentation models shown in **f**, **j**, and **m**, respectively. White arrows in **g** indicate a sheet adjacent to the hollow tube. (**h**, **i**) Tomographic slices of cross-sections h' and i' of the tubular structure shown in **g**. (**l**, **o**) Cross-sectional views of **k** and **n**, respectively. Diameters of the tubules shown in **d**, **h**, **l**, and **o** are 13, 14, 20, and 33 nm, respectively. Scale bar in **o** 50 nm (applies to **b**, **c**, **d**, **g**, **h**, **i**, **k**, **l**, **n**, **o**).